Optics Letters

Integrated visible light phased array system for autostereoscopic image projection

Manan Raval,* Ami Yaacobi, and Michael R. Watts

Research Laboratory of Electronics, Massachusetts Institute of Technology, Cambridge, Massachusetts 02141, USA
*Corresponding author: mraval@mit.edu

We demonstrate a chip-scale autostereoscopic image projection system that utilizes a system of multiple integrated visible light optical phased arrays to reconstruct virtual light fields. Each phased array in this system serves as a micro-projector that illuminates the desired virtual object from a different angle. This recreates the virtual object in space with continuous parallax observable by the human visual system. In this work, a static virtual image with horizontal parallax and a viewing angle of 5° was generated with an array of 16 integrated silicon nitride phased arrays with a 635 nm operating wavelength. Each phased array is comprised of 32×32 optical antennas with passively encoded relative phases. The presented device demonstrates the promise of integrated visible light phased array platforms for implementing projection-based autostereoscopic displays in compact chip-scale platforms suitable for mobile devices. © 2018 Optical Society of America

OCIS codes: (110.5100) Phased-array imaging systems; (130.3120) Integrated optics devices; (120.2040) Displays.

With increasing demand for three-dimensional (3D) media content, autostereoscopic display methods for mobile devices have recently attracted a great deal of interest [1–4]. An ideal glass-free 3D display provides all the depth cues required by the human visual system by exactly reproducing the light field of a virtual object. A light field may be generated using either a ray-based or wavefront-based method. The former is a geometric optics approach that involves directly reproducing the light rays from a virtual scene, whereas the latter constitutes a holographic approach that includes phase information from the virtual wavefront. While only holography can exactly reproduce the complex wave radiated from a 3D scene, its practical implementation currently faces some technical challenges. Practical holographic systems would benefit from the development of spatial light modulators with sufficiently high resolution, more efficient hologram computation methods, and the reduction of speckle noise [5,6]. Non-holographic 3D image projection methods, such as parallax barriers, lenticular sheets, and integral imaging, approximate light fields by concatenating multiple views of a virtual scene [6,7]. Smooth parallax cannot be achieved in these systems without the use of a large number of views, which requires a decrease in spatial resolution [8]. Additionally, depth range in a multi-view display system is achieved at the expense of image resolution [7–9]. In contrast, projection-based methods, in which an array of projectors is configured to illuminate a virtual light field, have been demonstrated with smooth parallax as well as high resolution and large viewing angle [10–14]. However, projection-based autostereoscopic systems presented to date utilize multiple discrete projector units. These are inherently bulky systems requiring precise physical alignment, thereby rendering them unsuitable for mobile applications [9,13,15].

Recently, integrated optical phased arrays have been demonstrated for projecting complex far-field patterns without any external optics [3,16]. Additionally, large-scale silicon- and silicon-nitride-based integrated optical phased arrays may be fabricated on 300 mm silicon wafers in standard CMOS foundries at high volume [17–19]. Integrated visible light phased arrays [20] would therefore facilitate the development of chip-scale projection-based light-field displays suitable for mobile devices. In this Letter, we demonstrate a system of multiple visible light integrated optical phased arrays for projecting a virtual image with horizontal parallax. A row of 16 32×32-emitter phased arrays are passively configured to project the light field of a virtual object. A ray-optics-based method is used for virtual object rendering [21]. This is, to the best of our knowledge, the first autostereoscopic image projection system based on integrated optical phased arrays demonstrated to date. Specifically, the photonic integrated circuit presented in this work demonstrates the ability to implement the functionality of multiple projectors for the direct reconstruction of virtual light fields on a single semiconductor chip fabricated in a CMOS-compatible process.

In light-field rendering, virtual objects may be represented as a collection of points in 3D space, or voxels. Multi-view displays typically do not employ a voxel discretization and project images corresponding to a set number of viewing zones, yielding smooth parallax only when a large number of views are available. Such displays therefore often exhibit stitching errors and image reversal at the edges of view zones, which prevents accurate depth cues and increases eye fatigue [4,6]. In contrast, projection-based autostereoscopic displays are configured with respect to the positions of voxels in physical space and can therefore deliver correct depth cues to any number of observers
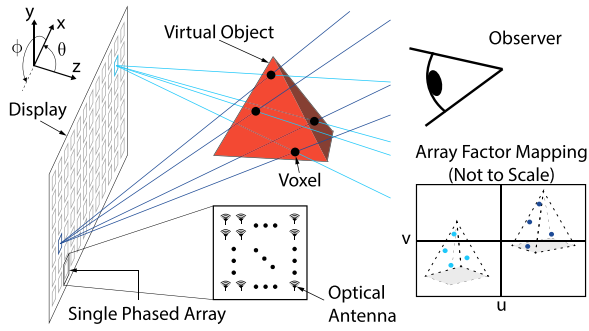
Fig. 1. Conceptual illustration of projection-based autostereoscopic image projection using optical phased arrays and voxel-to-array-factor mapping for two of the constituent phased arrays represented by dark and light blue markings.

within a single viewing zone [14,15,22]. Here, a dense array of projectors illuminates each voxel through a range of angles to approximate the behavior of a virtual point scatterer at the position of that voxel. A phased array may be used as a projector by appropriately configuring the phase and amplitude of each antenna to generate the desired image in its far field. This far-field diffraction pattern lies in an angular space and is defined by the array factor AF(θ,ϕ). The array factor is related to the near-field complex amplitude distribution ω_{mn} by a Fourier transform as

$$\mathrm{AF}(\theta,\phi) = \sum_{m=1}^{M}\sum_{n=1}^{N} \omega_{mn} e^{j2\pi(x_m u + y_n v)} = \mathcal{F}(\omega_{mn}), \quad \textbf{(1)}$$

where subscripts m and n refer to the antenna at location (x_m, y_n), $u = \sin\theta\cos\phi/\lambda$ and $v = \cos\theta\cos\phi/\lambda$ correspond to far-field coordinates where λ is wavelength, and $\mathcal{F}$ denotes the Fourier transform. Figure 1 conceptually illustrates autostereoscopic image projection using a multitude of phased arrays. Figure 1 also shows how a ray-optics-based algorithm [10,14] may be used to map voxels to the array factors of each phased array.

The 2D display configuration shown in Fig. 1 provides full parallax, but requires a large number of phased arrays. In a practical 3D display, the lack of vertical parallax is not a significant drawback, since human vision is dominated by horizontal motion [15,22]. A horizontal-parallax-only (HPO) configuration was therefore chosen in this work to demonstrate autostereoscopic functionality while maintaining a reasonably compact system footprint. This HPO configuration requires that an asymmetric diffuser with a large diffusion angle in the vertical dimension (y axis) and minimal diffusion in the horizontal dimension (x axis) be placed above the chip, as shown in Fig. 2. This allows viewers anywhere within the vertical diffusion range to observe the virtual image with all provided depth cues. Additionally, far-away observers may begin to see a set of vertical slices of the virtual image, each corresponding to a specific projector, with dark gaps in between [14,15]. The small horizontal diffusion angle θ_h will give these vertical image slices some horizontal extent, thereby filling in gaps with correct image information [15]. Image continuity is therefore achieved when the angle of separation between adjacent projectors is smaller than θ_h.

Figure 2 also shows the viewing volume and viewing angle θ_V as determined by the relevant display parameters. In projection-based autostereoscopy, these are generally determined

by the total display width and the range of angles through which light is emitted by each projector. In a system of phased array projectors, this angular range, or projection angle θ_p, is equal to the angular extent of a single diffraction order. The angular width of the 0th order is determined by the optical antenna pitch as $\theta_p = 2\sin^{-1}\frac{\lambda}{2d}$, where λ is wavelength, and d is the antenna pitch. For display width w_{disp}, projection angle θ_p, and image distance d_{im}, the maximum image width w_{im} is given by

$$w_{\mathrm{im}} = \frac{-4d_{\mathrm{im}} + \sqrt{16d_{\mathrm{im}}^2 + 4(4d_{\mathrm{im}}^2 + w_{\mathrm{disp}}^2)\tan(\theta_p)^2}}{2\tan(\theta_p)}, \quad \textbf{(2)}$$

where the image distance is defined as the z location at which the viewing volume has maximum width. The viewing angle θ_V is defined by w_{im}, w_{disp}, and d_{im}, as shown in Fig. 2. The extents of the viewing volume in z may then be defined with respect to w_{im} and the viewing angle, also as shown in Fig. 2. Any 3D surface defined in the viewing volume may be perceived with horizontal parallax by an observer in the viewing zone. The resolution of the virtual image is determined by the full width at half-maximum of the diffraction-limited beam divergence of each phased array, which in one dimension is defined as $\theta_d = 0.886\sin^{-1}\frac{\lambda}{Nd}$, where N is the number of emitters [23]. Therefore, any feature in the virtual image smaller than the diffraction-limited spot size at the location of the feature will not be resolved. Given this parameter space, one may consider a design example of a 2D display similar to that shown in Fig. 1 with a 102 mm × 56 mm screen size (approximately the size of the iPhone 7 screen) comprised of a 408 × 224 grid of 200 μm × 200 μm phased arrays with 250 μm center-to-center spacing in both dimensions. With an emitter pitch of 4 μm in both dimensions and an operating wavelength of 635 nm, this display can support a 3D image with a maximum viewing angle of 66° × 36° at an image height of approximately 6.6 cm above the screen.

The HPO autostereoscopic image projection system presented in this work is comprised of a one-dimensional array of 16 integrated optical phased arrays operating at a visible wavelength of 635 nm. Each phased array is comprised of 1024 optical antennas placed in a 32 × 32 grid with 4 μm pitch along both dimensions, resulting in a zeroth diffraction order width of 9.1°. Phased arrays are placed with a center-to-center
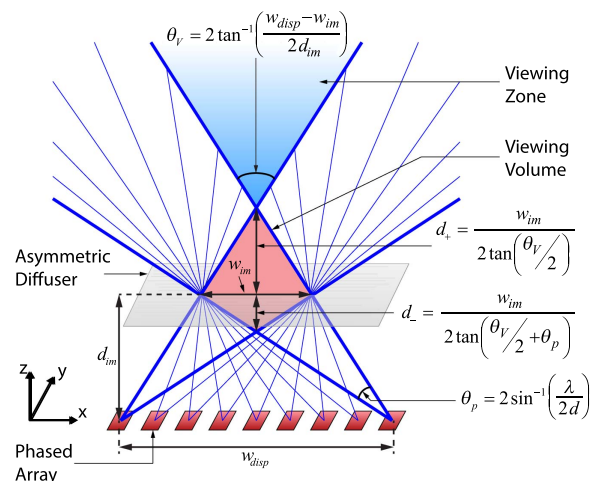
Fig. 2. Display configuration and parameters for a HPO phased-array-based autostereoscopic projection system.

spacing of 500 μm and configured to project a virtual image of a four-sided pyramid 30 mm above the chip with parallax in only the horizontal dimension. This results in a 5° viewing angle. The base of the pyramid forms a 30° angle with respect to the xz plane, and two of its faces are visible to the observer. Additionally, one of the faces is shaded to represent lighting from a specific direction.

As mentioned above, each phased array is encoded with a specific phase distribution for projecting the appropriate far-field radiation pattern corresponding to its location in the display. The far-field pattern of each phased array corresponds to the set of angles it must illuminate such that every point on the virtual 3D surface appears to radiate isotropically within the viewing zone. The phased array encoding process therefore begins with a discretization of the desired virtual image into a 3D collection of voxels in physical space. The target array factor of each phased array is then defined as the collection of angles (θ, ϕ) along which each voxel lies with the origin defined as the center of the phased array, as illustrated in Fig. 1. If the virtual surface is defined as a scalar field $V(x, y, z)$, the target array factor for a phased array at position (x_i, y_i) can be mapped as

$$AF_i(\theta, \phi) = \int_{-\infty}^{\infty} V_i\left(a, a \tan \phi, \frac{a}{\cos \phi \tan \theta}\right) \frac{1}{\cos \phi \sin \theta} da, \quad \text{(3)}$$

where $V_i = V(x - x_i, y - y_i, z)$ is the virtual image scalar field shifted in the xy plane to represent voxel locations relative to the position (x_i, y_i) of the ith phased array, and a is used to parameterize a straight line in the (θ, ϕ) direction.

While a simple inverse Fourier transform is often used to determine the necessary antenna configuration, the phased arrays presented in this work have uniform amplitude emission ($|\omega_{mn}| = 1$), such that only phase is encoded into each antenna. To overcome this constraint, the necessary phase distribution for each phased array for projecting its respective target array factor is calculated using the Gerchberg–Saxton (GS) algorithm similar to [16]. Higher-order images arise in the far field of an array with emitter pitch greater than $\frac{\lambda}{2}$, in which case the angular mapping of the array factor input to the GS algorithm is confined to zeroth diffraction order as $|u\lambda|$, $|v\lambda| \leq \frac{\lambda}{2d}$. As shown in Fig. 3(a), the target array factor calculated using Eq. (3) for phased arrays that are far from the center of the display may lie partially or entirely outside the zeroth diffraction order. In this case, excluded portions of the image are appropriately shifted by $(a\frac{\lambda}{d}, b\frac{\lambda}{d})$ in (u, v) space, where a and b are integers, such that all necessary image information is contained within a single diffraction order, as shown in Fig. 3(b), prior to calculating the corresponding phase distribution using the GS method. Figures 3(c) and 3(d) show the calculated phase distribution and array factor, respectively, for P2. Figure 3(e) shows the simulated array factors for three of the phased arrays. For the presented design, the uniform emission constraint and the finite emitter count prevent the GS algorithm from converging exactly to the target array factor, but a very close approximation is still achieved. In future iterations, arbitrary amplitude encoding and higher emitter counts may be implemented for increasing virtual image resolution and fidelity [24,25] while aperiodic emitter spacing could be used to suppress higher diffraction orders [17].

The presented display system was patterned in a 200 nm thick silicon nitride layer using 193 nm UV immersion lithography with silicon dioxide cladding on a 300 mm silicon wafer.
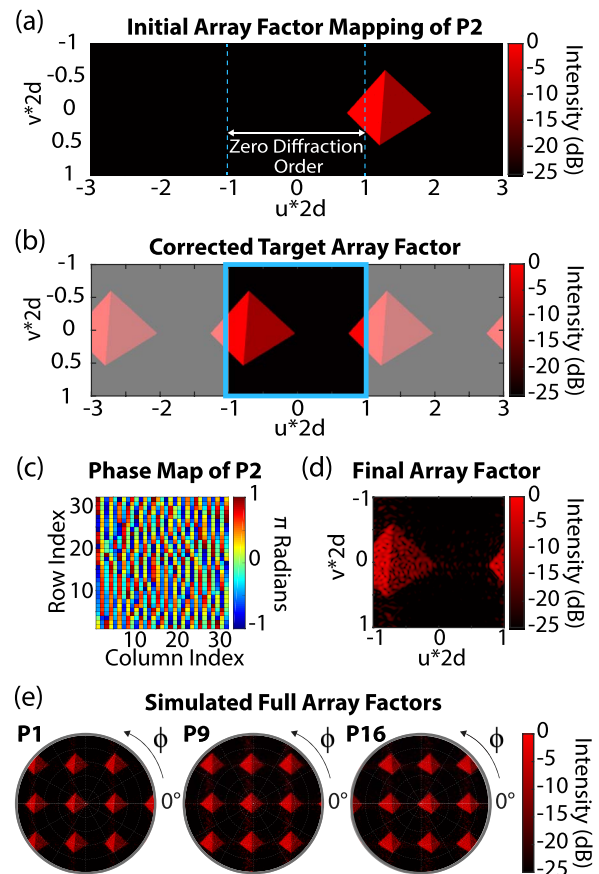

Fig. 3. (a) Initial array factor mapping to (u, v) space for phased array P2 located at $x = -3.25$ mm. (b) Target array factor for P2 after shifting excluded sections of the image into the zeroth diffraction order (outlined in blue). (c) Phase map of antennas and (d) array factor calculated using the GS algorithm with the target array factor from (b). (e) Expanded array factors of P1, P9, and P16 showing higher diffraction orders.

Figure 4(a) shows an optical micrograph of the full image projection device, and Fig. 4(b) shows a schematic of the passive phased array architecture. Light from a 635 nm fiber-coupled diode laser is edge coupled into a display bus waveguide. Light is then coupled to each phased array via a series of directional couplers whose lengths are increased along the display bus waveguide to deliver an equal amount of light to each phased array. Light in each phased array is then delivered to each row of antennas and subsequently to each unit cell in a similar manner to uniformly illuminate the array [16]. Each unit cell includes a directional coupler to tap light from a bus waveguide and a grating-based optical antenna to couple light to free space, as shown in Fig. 4(c). Additionally, a 60 nm offset between the straight and curved regions of the unit cell waveguide compensates for mode mismatch between the two regions [26]. The phase of each antenna is passively encoded by shifting its position along its corresponding row bus waveguide relative to a default location defined by a 4-μm-pitch grid, as illustrated in Fig. 4(c). To achieve a full 2π phase shift, the unit cell may be displaced by up to $\pm \frac{\lambda}{2n_{\text{eff}}}$, where n_{eff} is the effective index of the row bus waveguide. Since this displacement is of significantly lower magnitude than the unit cell pitch, any resulting noise in the array factor is negligible.
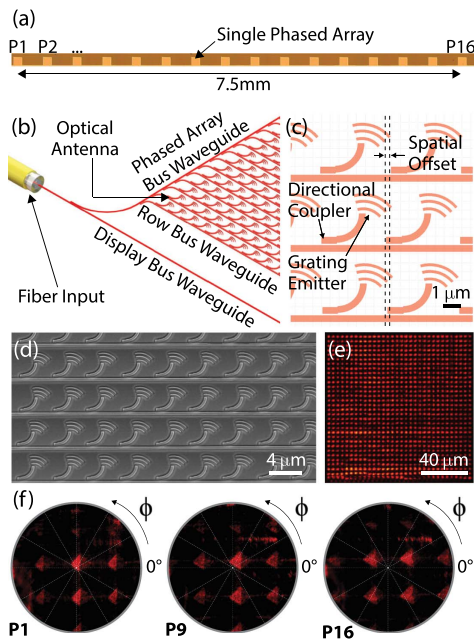
Fig. 4. (a) Optical micrograph of the image projection system. (b) Passive phased array architecture. (c) Schematic of optical antenna arrangement with passive phase encoding by means of spatial offsets in unit cell placement. (d) SEM of a section of a phased array. (e) Camera image of the near-field emission profile of one of the phased arrays. (f) Camera images of the individual far fields of phased arrays P1, P9, and P16.

Figure 4(e) shows an image of the near field of one of the phased arrays, in which a highly uniform emission profile is achieved using the aforementioned light distribution system based on cascaded directional couplers. Measured far-field radiation patterns of three of the phased arrays in the display are shown in Fig. 4(f). Camera images of the virtual object projected by the system are shown in Fig. 5. A Thorlabs 0.4° × 100° line diffuser (ED1-L4100) was used as the asymmetric diffuser. When imaging the virtual object, a lens with a focal length of 60 mm was placed approximately 10 mm above the asymmetric diffuser to slightly magnify the image to aid in the imaging process. The camera images in Fig. 5 display the virtual object as it would appear to an observer from three different perspectives (left, center, right) within the viewing zone. Horizontal parallax can be observed in Fig. 5 as the perspective moves across the viewing zone from left to right. Higher diffraction orders also form duplicate virtual objects that exhibit parallax. However, higher diffraction orders correctly align to form virtual objects only for small angles.
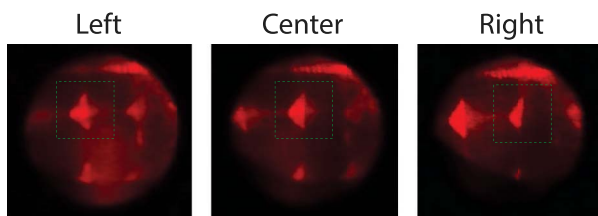
In conclusion, we have presented the design process and a first demonstration of projection-based autostereoscopy using a system of multiple integrated optical phased arrays. A one-dimensional array of 16 silicon-nitride phased arrays designed for 635 nm operation was passively configured to project the light field of a virtual pyramid with horizontal parallax. This photonic circuit was fabricated on a 300 mm wafer in a CMOS foundry, thereby making scaling to larger display sizes for larger viewing angle and higher resolution straightforward. Furthermore, integration of electro-optic materials such as liquid crystals [27] in the future would enable the development of actively configurable integrated visible light phased array systems for 3D video devices.

REFERENCES

1. D. Fattal, Z. Peng, T. Tran, S. Vo, M. Fiorentino, J. Brug, and R. G. Beausoleil, Nature **495**, 348 (2013).
2. A. Markman, J. Wang, and B. Javidi, Optica **1**, 332 (2014).
3. F. Aflatouni, B. Abiri, A. Rekhi, and A. Hajimiri, Opt. Express **23**, 21012 (2015).
4. G.-J. Lv, B.-C. Zhao, F. Wu, W.-X. Zhao, Y.-Z. Yang, and Q.-H. Wang, Appl. Opt. **56**, 2792 (2017).
5. F. Yaras, H. Kang, and L. Onural, J. Disp. Technol. **6**, 443 (2010).
6. M. Yamaguchi, J. Opt. Soc. Am. A **33**, 2348 (2016).
7. J. Geng, Adv. Opt. Photon. **5**, 456 (2013).
8. S. Gi Park, J. Yeom, Y. Jeong, N. Chen, J.-Y. Hong, and B. Lee, J. Inf. Disp. **15**, 37 (2014).
9. S. Gi Park, J.-Y. Hong, C.-K. Lee, M. Miranda, Y. Kim, and B. Lee, Appl. Opt. **53**, G198 (2014).
10. A. Jones, I. McDowall, H. Yamada, M. Bolas, and P. Debevec, ACM Trans. Graph. **26**, 40 (2007).
11. Y. Peng, H. Li, Q. Zhong, and X. Liu, Appl. Opt. **51**, 6014 (2012).
12. C.-K. Lee, S. Gi Park, S. Moon, J.-Y. Hong, and B. Lee, Opt. Express **23**, 28945 (2015).
13. T. Balogh, Proc. SPIE **6055**, 60550U (2006).
14. Q. Zhong, Y. Peng, H. Li, C. Su, W. Shen, and X. Liu, Appl. Opt. **52**, 4419 (2013).
15. A. Jones, K. Nagano, J. Liu, J. Busch, X. Yu, M. Bolas, and P. Debevec, J. Electron. Imaging **23**, 011005 (2014).
16. J. Sun, E. Timurdogan, A. Yaacobi, E. S. Hosseini, and M. R. Watts, Nature **493**, 195 (2013).
17. D. N. Hutchison, J. Sun, J. K. Doylend, R. Kumar, J. Heck, W. Kim, C. T. Phare, A. Feshali, and H. Rong, Optica **3**, 887 (2016).
18. C. V. Poulton, A. Yaacobi, D. B. Cole, M. J. Byrd, M. Raval, D. Vermeulen, and M. R. Watts, Opt. Lett. **42**, 4091 (2017).
19. M. Raval, C. V. Poulton, and M. R. Watts, Opt. Lett. **42**, 2563 (2017).
20. C. V. Poulton, M. J. Byrd, M. Raval, Z. Su, N. Li, E. Timurdogan, D. Coolbaugh, D. Vermeulen, and M. R. Watts, Opt. Lett. **42**, 21 (2017).
21. M. Levoy and P. Hanrahan, SIGGRAPH (ACM, 1996), pp. 31–42.
22. J.-H. Lee, J. Park, D. Nam, S. Y. Choi, D.-S. Park, and C. Y. Kim, Opt. Express **21**, 26820 (2013).
23. K. V. Acoleyen, W. Bogaerts, J. Jágerská, N. L. Thomas, R. Houdré, and R. Baets, Opt. Lett. **34**, 1477 (2009).
24. J. Sun, E. Shah Hosseini, A. Yaacobi, D. B. Cole, G. Leake, D. Coolbaugh, and M. R. Watts, Opt. Lett. **39**, 367 (2014).
25. J. Zhou, J. Sun, A. Yaacobi, C. V. Poulton, and M. Watts, Advanced Photonics (Optical Society of America, 2015), paper IT4A.7.
26. E. G. Neumann, IEE Proc. H **129**, 278 (1982).
27. Y. Xing, T. Ako, J. P. George, D. Korn, H. Yu, P. Verheyen, M. Pantouvaki, G. Lepage, P. Absil, A. Ruocco, C. Koos, J. Leuthold, K. Neyts, J. Beeckman, and W. Bogaerts, IEEE Photon. Technol. Lett. **27**, 1269 (2015).

Fig. 5. Camera images of the fully illuminated system with the asymmetric diffuser placed above the chip.